Hindawi
International Journal of Energy Research
Volume 2024, Article ID 1386237, 21 pages
https://doi.org/10.1155/2024/1386237

WILEY | Hindawi

Research Article

Theoretical Analysis of the Power Performance of a Monostable Galloping-Based Piezoelectric Energy Harvester

Lu Zhang, Chunbo Lan, Fangjie Lu, and Yang Lu

College of Aerospace Engineering, Nanjing University of Aeronautics and Astronautics, Nanjing, China

Correspondence should be addressed to Chunbo Lan; chunbolan@nuaa.edu.cn

Received 5 September 2023; Revised 29 January 2024; Accepted 9 February 2024; Published 20 March 2024

Academic Editor: Mumtaz Ahmad Qaisrani

In the past few years, different kinds of structural nonlinearities, such as external magnetic interaction and multistable structures, have been introduced into galloping energy harvesters to enhance energy harvesting efficiency. However, since the galloping-based piezoelectric energy harvester (GPEH) is a self-excited system, the conventional impedance matching method that is widely used in vibration energy harvesters is no longer valid for it. Therefore, the power characteristics of the nonlinear GPEH are still an open question to be solved. To this end, this paper is motivated to derive the approximate analytical solution of a monostable galloping-based piezoelectric energy harvester through the harmonic balance method and impedance matching theory. The analytical maximum power, power limit, and critical electromechanical coupling are studied from the perspective of the influence of structural nonlinearity on the power performance. Firstly, the approximate analytical solutions of output power, power limit, optimal resistance, and critical electromechanical coupling coefficient are derived. The accuracy of the analytical solution is verified by numerical simulation. It is found that the influence of structural nonlinearity on the power characteristics of the nonlinear GPEH is quite different under different wind speeds. After that, the power characteristics of the system under different wind speeds and different coupling conditions are investigated. The results showed that the maximum power of the system can be increased by introducing stiffness nonlinearity under low wind speed and weakly coupled configuration. Even more, the system can be shifted into a strongly coupled system when the nonlinearity is enhanced to a certain level. Reasonable design of stiffness nonlinearity can effectively reduce the critical electromechanical coupling, which indicates that stiffness nonlinearity is a feasible and effective way to improve the power performance of low-speed wind energy harvesting.

1. Introduction

In recent years, wireless sensor network (WSN) has been widely used in the Internet of Things (IoT), smart homes, information management systems, and other emerging fields. The demand for wireless sensors and other microelectronic devices in our daily lives increases day by day. The power supply of these wireless sensors in IoT is a big challenge. Energy harvesting from the ambient environment has been a promising way to provide a continuous power supply for these small devices [1–5]. Wind energy is one of the most stable, environmentally friendly, and sustainable energy sources. Among a variety of wind energy harvesters [6–8], galloping-based energy harvester stands out because it can yield a considerable power output at small wind speed scenarios [9, 10].

The feasibility of galloping-based energy harvesting was first experimentally validated by Barrero-Gil et al. [11]. Then, Sirohi and Mahadik [12] derived a simplified model for galloping energy harvester. After that, more and more efforts have been devoted to the research of galloping energy harvesting [13–15]. Abdelkefi et al. [16] found that the electrical load resistance and Reynolds number can affect the onset wind speed of galloping, and the maximum output power is accompanied by the minimum transverse displacement regardless of the Reynolds number.

With the quick development on galloping energy harvesters, the methods to improve its output power, including

bluff body design/optimization, advanced energy harvesting circuits, and structural nonlinearity, have become new research topics. For example, researchers have made many innovations in the design of bluff body shapes [17, 18]. Yang et al. [19] found that when the wind speed is low, the bluff body with a square cross-section can improve the output power significantly. Abdelkefi et al. [20] established a coupled nonlinear distributed-parameter model for a galloping energy harvester and found that when the wind speed was relatively high, the D-shaped section was the optimal choice over other shapes. After that, Liu et al. [21] proposed a forked bluff body. Both experimental and simulation results show that the output power can be effectively improved.

Meanwhile, some researchers have been concentrating on concurrent energy harvesting. For example, Yang et al. [22] developed a distributed-parameter electromechanical coupling model of a VIV-galloping interactive energy harvester and found that the performance of the system at low wind speeds is significantly improved when vortex-induced vibration interacts with galloping-induced vibration. Hu et al. [23] investigated the optimal relative position of two galloping-based energy harvesters that were placed adjacently and interacting with each other in tandem or staggered arrangements. Kim et al. [24] proposed a novel galloping-based piezoelectric energy harvester coupled with transverse and interference galloping, which can harvest 20 times more energy than the conventional configuration.

Inspired by the success of nonlinear vibration energy harvesting, structural nonlinearity was introduced into the galloping energy harvester as well. Bibo et al. [25] studied the effect of nonlinearity on the performance of the monostable/bistable galloping energy harvesters. Huang et al. [26] proposed a 2-DOF tristable dynamic vibration absorber and energy harvester, finding that a tristable electromagnetic energy harvester has favorable energy trapping capacity and energy conversion performance under broadband and low-amplitude vibrations. Wang et al. [27] experimentally found that the maximum output power of a tristable galloping-based energy harvester reached 0.73 mW and the cut-in wind speed was 1 m/s. Alhadidi and Daqaq [28] observed that exploiting a bistable restoring force can improve the lock-in region of a wake galloping-based energy harvester, and the steady-state bandwidth of a bistable system is wider than the conventional linear system.

Since the galloping energy harvester is a self-excitation system, its equivalent circuits do not have a power supply. Therefore, the conventional impedance matching method widely used in vibration energy harvester is no longer suitable for deriving analytical solutions for galloping energy harvester. Therefore, although lots of structural nonlinearities were claimed to have the capability of improving the maximum power of galloping energy harvesting [29–32], the power limit problem of these nonlinear galloping energy harvesters was rarely studied. Therefore, a new theoretical analysis method is urgently needed to investigate the power characteristics of galloping-based energy harvesters. To this end, Lan et al. [33] proposed a unified impedance matching framework for the galloping energy harvester based on the harmonic balanced method and Kirchhoff law, obtaining the analytical solutions of the optimal load, maximum power, power limit, and critical electromechanical coupling and analyzing power performance of galloping-based energy harvesters with different interface circuits. Although a thorough analysis of the power performances of galloping-based energy harvesters was conducted, they only focused on linear systems. In this paper, we mainly focused on the power limit characteristics of nonlinear galloping energy harvesters by using the unified impedance matching method and tried to ascertain the inherent role of structural nonlinearity on power limit characteristics.

The presence of nonlinear magnetic repulsion introduces structural nonlinearity, resulting in distinct power characteristics at different wind speeds. Therefore, this study investigates the impact of structural nonlinearity on the power performance of the system under varying wind speeds and electromechanical coupling conditions. Through numerical solutions, theoretical analysis, and simulations, the system's response is systematically examined. Analytical approximations for the maximum power, power limit, optimal resistance, and critical coupling of a monostable galloping-based energy harvester interfaced with an AC circuit are derived. The influence of stiffness nonlinearity on maximum power, power limit, and critical coupling is determined. This comprehensive research provides new insights and a research framework for designing nonlinear monostable galloping-based energy harvesters. The rest of this work is organized as follows: Section 2 introduces the model of a monostable energy harvester. Section 3 established the equivalent circuit and derived the approximate analytical solution of output power by using the unified impedance match method [34, 35]. Numerical validation was also included. After that, the power performance of a monostable GPEH was deeply studied in Section 4 with some useful conclusion drawn in Section 5.

2. Modeling and Equivalent Circuit

2.1. A Monostable Galloping-Based Energy Harvester. Figure 1 shows the schematic of the monostable galloping-based energy harvester in this paper. It consists of a piezoelectric cantilever beam, a foam bluff body, and two magnets. The piezoelectric patch is fixed at the root of the cantilever beam to convert mechanical energy into electrical energy. One of the magnets is fixed on the bottom wall, while the other magnet is placed opposite to it and fixed on the free end of the cantilever beam. Therefore, the magnets with the same magnetism can produce a nonlinear magnetic repulsive force. The bluff body is fixed at the end of the cantilever beam, and the nonlinear aerodynamic force induced by flow acts on its surface. The cross-section of the bluff body used in this paper is semicircular since it is found that the output power of the system with a semicircular bluff body is relatively stable [16]. When the wind speed exceeds a critical value, the bluff body undergoes transverse oscillations, called the galloping phenomenon.

2.2. Modeling. For the nonlinear galloping-based energy harvester shown in Figure 1, the governing equations can be

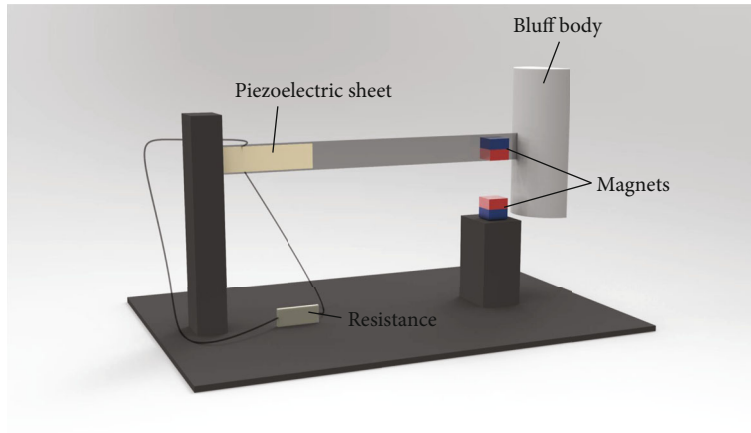

Figure 1: Illustration of a monostable galloping energy harvester.

obtained by the assumption of linear electromechanical coupling and elasticity [11]. They can be written as

$$M\ddot{x}(t) + C\dot{x}(t) + Kx(t) + k_1x(t) + k_3x^3(t) - \theta v_p = F_a,$$
$$\theta\dot{x}(t) + C_p\dot{v}_p(t) + \dot{q}(t) = 0, \quad (1)$$

where M, C, and K are the effective mass, effective damping, and effective stiffness, respectively. The effective damping can be expressed as $C = 2\zeta\omega_n M$, where ζ is the damping ratio, ω_n is the natural frequency, θ is the electromechanical coupling coefficient, C_p is the capacitance of the piezoelectric transducer, k_1 and k_3 represent the effect of magnetic repulsion, x is the displacement, $\dot{x}$ is the speed, $\ddot{x}$ is the acceleration, v_p is the voltage across the piezoelectric element (that is, the external energy harvesting interface circuit), q is the charge, and F_a is the vertical component of the aerodynamic force acting on the bluff body. In this paper, the experimentally verified cantilever beam model developed by Liao and Sodano [36] is used, for which the effective system parameters have been obtained

$$M = \int_{V_s} \rho_s\varphi\varphi \mathrm{d}V_s + \int_{V_p} \rho_p\varphi\varphi \mathrm{d}V_p + M_t,$$
$$K = \int_{V_s} y^2\varphi'' c_s\varphi'' \mathrm{d}V_s + \int_{V_p} y^2\varphi'' c_p^E\varphi'' \mathrm{d}V_p,$$
$$\theta = -\int_{V_p} y\varphi'' e^T\psi \mathrm{d}V_p, \quad (2)$$
$$C_p = \int_{V_p} \psi^T\varepsilon^S\psi \mathrm{d}V_p,$$

where ρ is the density, c is the elastic modulus, ε is the dielectric constant, e is the piezoelectric coupling coefficient, and M_t is the mass of the tip mass. The subscripts p and s denote piezoelectric materials and substrates, respectively. The superscript $()^S$ represents the parameter measured at constant strain. The superscript $()^T$ indicates the parameter measured under constant stress. The superscript $()^E$ donates the parameter measured under a constant electric field. φ is the vibration mode shape, and ψ represents the electric field over the thickness of the piezoelectric transducer, which is assumed to be constant.

The dipole-dipole model has been widely used in the modeling of monostable and bistable systems [37], and its accuracy has been verified by experiments and has been widely used in previous studies. In Eq. (1), the sum of the two terms $k_1x(t)$ and $k_3x^3(t)$ represents the nonlinear interaction force between the two repulsive magnets, which is the Taylor expansion of the nonlinear magnetic repulsion force at $x = 0$ after modeling based on the dipole-dipole assumption. It should be noted that the discrepancy induced by Taylor expansion is very limited and acceptable when the system response is not very large at low wind speed condition. When the wind speed is large enough to achieve a large response, such an approximation may result in a large discrepancy. After omitting the higher-order term, the nonlinear magnetic force can be approximated as [36, 38]

$$F_m = k_1x + k_3x^3,$$
$$k_1 = -\frac{\bar{m}_A\bar{m}_B\bar{v}_A\bar{v}_B\mu_0}{4\pi}\frac{12}{D_0^5}, \quad (3)$$
$$k_3 = \frac{\bar{m}_A\bar{m}_B\bar{v}_A\bar{v}_B\mu_0}{4\pi}\frac{45}{D_0^7},$$

where μ_0 is the vacuum permeability, D_0 is the initial center-to-center distance between the two magnets, $\bar{m}_A$ and $\bar{m}_B$ are the magnitude of the magnetization vector, and $\bar{v}_A$ and $\bar{v}_B$ are the volumes of the two magnets. It is verified that the approximate magnetic force value in Eq. (3) is very close to the exact result. It can be seen from the above expression that

the smaller the distance between the two magnets, the larger the absolute value of the nonlinear coefficients k_1 and k_3, and the nonlinear effect is also enhanced.

For galloping-based energy harvesters, aerodynamic force is generally modeled following the quasisteady assumption. The quasisteady assumption holds that compared with the wind speed acting on the bluff body, the speed of the bluff body is very slow. Therefore, for a given angle of attack, the aerodynamic coefficient remains constant. According to the study of Barrero-Gil et al. [11], the aerodynamic force F_a can be modeled as

$$F_a = \frac{1}{2}\rho LDU^2\left[s_1\frac{\dot{x}}{U} - s_3\left(\frac{\dot{x}}{U}\right)^3\right], \tag{4}$$

where L and D are the length and width of the bluff body, respectively. ρ and U are air density and wind speed, respectively. s_1 and s_3 are the empirical linear coefficients and cubic coefficients of aerodynamic force, which only depend on the cross-section geometry of the prismatic structure. Substituting Eq. (4) into Eq. (1), then the governing equation of the system can be written as

$$\begin{aligned} M\ddot{x} + C\dot{x} + (K + k_1)x + k_3x^3 - \theta v_p &= \frac{1}{2}\rho LDU\left[s_1\dot{x} - \frac{s_3}{U^2}(\dot{x})^3\right], \\ \theta\dot{x} + C_p\dot{v}_p + \dot{q} &= 0. \end{aligned} \tag{5}$$

3. Approximate Solution of Maximum Power and Power Limit

3.1. Equivalent Circuit. First, the equivalent circuit method is used to represent the electromechanical system in the electrical domain. In the equivalent circuit method, the physical parameters in the system can be fully described by the electric parameters, so the whole system can be equivalent to a circuit. In order to derive the equivalent circuit model, the nonlinear aerodynamic force and nonlinear magnetic repulsion force should be linearized first by using the harmonic balance method. Based on the assumption of the harmonic balance method, the solution of Eq. (5) could be written as

$$\begin{aligned} x &= a\sin\omega t + b\cos\omega t, \\ \dot{x} &= a\omega\cos\omega t - b\omega\sin\omega t, \end{aligned} \tag{6}$$

where ω is the vibration frequency of the system and a and b are the structural response constants.

By using the trigonometric function formula and ignoring the higher-order harmonic terms in the results, we can get the results as (The detailed derivation is given in the Appendix.)

$$\begin{aligned} x^3 &= (a\sin\omega t + b\cos\omega t)^3 \approx \frac{3}{4}r^2x, \\ \dot{x}^3 &= (a\omega\cos\omega t - b\omega\sin\omega t)^3 \approx \frac{3}{4}\omega^2r^2\dot{x}, \end{aligned} \tag{7}$$

where r is the responding amplitude of the system, i.e.,

$$r^2 = a^2 + b^2. \tag{8}$$

Substituting Eqs. (7) and (8) into Eq. (5), the governing equation is approximately equivalent as follows:

$$\begin{aligned} M\ddot{x} + C\dot{x} + (K + k_1)x + \frac{3}{4}k_3r^2x - \theta v_p &= \frac{1}{2}\rho LDU\left(s_1 - \frac{3s_3\omega^2r^2}{4U^2}\right)\dot{x}, \\ \theta\dot{x}(t) + C_p\dot{v}_p(t) + \dot{q}(t) &= 0. \end{aligned} \tag{9}$$

The first expression of Eq. (9) can be written as

$$M\ddot{x} + C\dot{x} - \frac{1}{2}\rho LDUs_1\dot{x} + \frac{3\rho LDs_3\omega^2r^2}{8U}\dot{x} + (K + k_1)x + \frac{3}{4}k_3r^2x - \theta v_p = 0. \tag{10}$$

To further obtain the equivalent circuit equation of the system, we define the equivalent current $i_{eq} = -\theta\dot{x}$ here and rewrite Eq. (10) into an expression containing the equivalent current i_{eq}. Then, Eq. (10) can be written as

$$\begin{aligned} &\frac{M}{\theta^2}\frac{d(-\theta\dot{x})}{dt} + \frac{C}{\theta^2}(-\theta\dot{x}) - \frac{\rho LDUs_1}{2\theta^2}(-\theta\dot{x}) + \frac{3\rho LDs_3\omega^2r^2}{8U\theta^2}(-\theta\dot{x}) \\ &\quad + \frac{(K + k_1)}{\theta^2}\int(-\theta\dot{x})dt + \frac{3k_3r^2}{4\theta^2}\int(-\theta\dot{x})dt + v_p = 0. \end{aligned} \tag{11}$$

Equation (11) can be further written as

$$L_s\frac{di_{eq}}{dt} + R_si_{eq} + R_1i_{eq} + R_3i_{eq} + C_s\int i_{eq}dt + C_n\int i_{eq}dt + v_p = 0. \tag{12}$$

Equation (12) is an equivalent voltage equation, which means the energy harvesting system has been equivalent to a closed circuit now. According to Kirchhoff's voltage law, the first six terms in Eq. (12) are the equivalent voltage drop of the energy harvester, and the last term is the voltage of the load impedance. Here, we have equated the energy harvester to one equivalent inductance, three equivalent resistances, and two capacitances. By comparing Eqs. (11) and (12), the equivalent circuit elements can be defined as

$$
\begin{aligned}
L_s &= \frac{M}{\theta^2},\\
R_s &= \frac{C}{\theta^2},\\
R_1 &= -\frac{\rho LDUs_1}{2\theta^2},\\
R_3 &= \frac{3\rho LDs_3\omega^2 r^2}{8U\theta^2},\\
C_s &= \frac{\theta^2}{(K+k_1)},\\
C_n &= \frac{4\theta^2}{3k_3 r^2},
\end{aligned}
\tag{13}
$$

where L_s, R_s, and C_s correspond to the equivalent mass, equivalent damping, and equivalent stiffness of the energy harvester, respectively, R_1 and R_3 represent the influence of aerodynamic force, and C_n represents the influence of magnetic repulsion. The equivalent circuit diagram of the system at this time is shown in Figure 2. The analytical solution of the equivalent circuit has been verified by simulation and experiment in Ref. [39, 40]. C_p is the capacitance of the piezoelectric transducer. When a piezoelectric energy harvester is equivalent to a circuit, it is connected in parallel with load resistance as part of the load impedance [33].

3.2. Maximum Power. The general form of the load circuit impedance is as

$$
Z_{\text{elec}} = R_{\text{elec}} + jX_{\text{elec}}, \tag{14}
$$

where R_{elec} and X_{elec} represent the resistance component and reactance component, respectively. The impedance is not only related to the load impedance but also affected by the internal circuit of the energy harvester. When the system parameters are determined, the equivalent impedance is only related to the load impedance of the interface circuit. The interface circuit selected in this paper only contains a resistance R. When R changes, Z_{elec} changes accordingly. As shown in Figure 2, the equivalent circuit of the system is obviously a self-excited circuit, so the voltage drop of the whole loop must be zero. Based on the information known above, we can rewrite Eq. (12) as the voltage relationship in the frequency domain forms

$$
\left[j\omega L_S + R_s + R_1 + R_3 + \frac{1}{j\omega C_s} + \frac{1}{j\omega C_n} + Z_{\text{elec}}(j\omega)\right] i_{eq}(j\omega) = 0. \tag{15}
$$

When galloping occurs, the equivalent current of the system could not be zero. Hence, the sum of the items in the bracket should be zero. Then, substituting Eq. (11) into Eq. (12), it can be obtained that

$$
\begin{aligned}
\omega L_s - \frac{1}{\omega C_s} - \frac{1}{\omega C_n} + X_{\text{elec}} &= 0,\\
R_s + R_1 + R_3 + R_{\text{elec}} &= 0.
\end{aligned}
\tag{16}
$$

These two expressions are the imaginary part and the real part, respectively. Substitute the expressions of electrical components in the equivalent circuit model of the system into Eq. (16), we can get

$$
\begin{aligned}
\omega^2 M - (K+k_1) - \frac{3}{4}k_3 r^2 + \theta^2\omega X_{\text{elec}} &= 0,\\
\frac{C}{\theta^2} - \frac{\rho LDUs_1}{2\theta^2} + \frac{3\rho LDUs_3\omega^2 r^2}{8U^2\theta^2} + R_{\text{elec}} &= 0.
\end{aligned}
\tag{17}
$$

The response frequency and amplitude of the system can be obtained from Eq. (17). It is not hard to see that when galloping occurs, the resonance frequency and amplitude are not only related to the original mechanical parameters but also influenced by the interface circuit. Hence, only when the energy harvesting circuit and load characteristics, i.e., R_{elec} and X_{elec}, are determined, the structural response can be calculated by Eq. (17).

3.3. Power Limit. The harvested power of the GPEH, i.e., dissipated in the external energy harvesting circuit, can be calculated by

$$
P = {i_{eq}}^2 R_{\text{elec}} = |-\theta\dot{x}|^2 R_{\text{elec}} = \theta^2\omega^2 r^2 R_{\text{elec}}. \tag{18}
$$

Interestingly, it can be obtained from the second expression of Eq. (17) that $\omega^2 r^2 = (4\rho LDU^2 s_1 - 8CU - 8UR_{\text{elec}}\theta^2)/3\rho LDs_3$. Substituting it into Eq. (18) yields the harvested power for a GPEH in general:

$$
\begin{aligned}
P &= \frac{\theta^2 R_{\text{elec}}}{3\rho LDs_3}\left(4\rho LDU^2 s_1 - 8CU - 8UR_{\text{elec}}\theta^2\right)\\
&= \frac{8U\theta^4}{3\rho LDs_3}\left[-{R^2}_{\text{elec}} + \left(\frac{\rho LDUs_1 - 2C}{2\theta^2}\right)R_{\text{elec}}\right]\\
&= \frac{8U\theta^4}{3\rho LDs_3}\left[-\left(R_{\text{elec}} - \frac{\rho LDUs_1 - 2C}{4\theta^2}\right)^2 + \left(\frac{\rho LDUs_1 - 2C}{4\theta^2}\right)^2\right].
\end{aligned}
\tag{19}
$$

It can be clearly seen from Eq. (19) that the output power of the system is only related to the resistance component R_{elec} of the impedance, while the reactance component X_{elec} can affect the galloping frequency of the system. More importantly, only effective damping C of the three original mechanical parameters appears in the expression of output power.

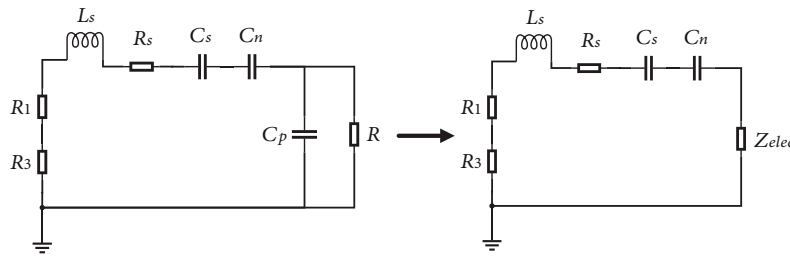

Figure 2: Equivalent circuit diagram of a GPEH interfaced with an AC circuit.

It can be seen from Eq. (19) that when the resistance R_{elec} satisfies the following conditions:

$$R_{\text{elec}} = \frac{\rho LDUs_1 - 2C}{4\theta^2}, \tag{20}$$

the output power reaches its maximum, which is the power limit of the system.

The power characteristics of the system will be analyzed in the following section. Notably, R_0 is defined as

$$R_0 = \frac{\rho LDUs_1 - 2C}{4\theta^2}. \tag{21}$$

The analytical solution of the system power limit can be obtained as follows:

$$P_{\text{lim}} = \frac{8U\theta^4}{3\rho \text{LD}s_3}\left(\frac{\rho LDUs_1 - 2C}{4\theta^2}\right)^2. \tag{22}$$

3.4. Numerical Validation

3.4.1. Model Validation. In Section 3.1, an analytical solution for the monostable galloping-based energy harvester was derived using the harmonic balance method. However, the derivation process neglected higher-order harmonic terms, which is a major source of error in the harmonic balance method. To verify the accuracy of the analytical solution, it was compared with the numerical results obtained using the Runge-Kutta method. The distance between the magnets in the calculation is 17.5 mm and 50 mm, respectively. The nonlinear coefficients corresponding to the two magnet distances are $k_1 = -15\,\text{N/m}$, $k_3 = 1.9 \times 10^5\,\text{N/m}^3$, $k_1 = -0.08$ N/m, and $k_3 = 119\,\text{N/m}^3$, respectively. The resistance R is $6\,\text{k}\Omega$, and the electromechanical coupling coefficient is 1.5×10^{-4} N/V. The displace diagrams calculated by the two methods are shown in Figure 3, and it is evident that the analytical results are in good agreement with the numerical simulation results. Figure 3 illustrates that when the magnet distance D_0 is 50 mm, the analytical results are basically consistent with the numerical simulation results calculated by the Runge-Kutta method. When the distance between the two magnets is reduced to 17.5 mm, the error between the analysis results and the numerical solution is slightly increased, but the variations of the displacement with wind speed are still consistent. In addition, by comparing the system response of $D_0 = 50$ mm and $D_0 = 17.5$ mm, it can be found that when the wind speed is about 2 m/s to 2.8 m/s, the enhancement structural nonlinearity leads to the increase of the displacement, while when the wind speed is outside this range, the nonlinear enhancement leads to the weakening of the system response. Then, based on this finding, two sets of wind speeds, 2.3 m/s and 3.5 m/s, are selected to further explore the effect of structural nonlinearity on the response of a GPEH. Figures 4 and 5 give the time-domain response diagram and phase diagram when the wind speed is 2.3 m/s and 3.5 m/s, respectively. It can be seen that when D_0 is 17.5 mm, the displacement and velocity of the system are larger than that when D_0 is 50 mm. In other words, at the wind speed of 2.3 m/s, the enhancement of structural nonlinearity causes the enhancement of the vibration response of the system, and the output power also increases. When the wind speed increases to 4 m/s, as shown in Figure 5, the displacement and the velocity at $D_0 = 17.5$ mm are smaller than that when D_0 is 50 mm, which is different from that when the wind speed is 2.3 m/s. This indicates that with the enhancement of structural nonlinearity, the vibration of the system is weakened, and the output power is also decreased. The result is consistent with that shown in Figure 3. When the wind speed is low, the structural nonlinearity can enhance the system response and increase the output power. Instead, when the wind speed increases to a certain level, the vibration response of the system will be suppressed and the output power can be reduced. It can be inferred that at small wind speed, introducing structural nonlinearity is an effective way to improve the power characteristics of the system.

3.4.2. Numerical Validation. The analytical solution of the maximum output power of the system has been obtained by using the nonlinear impedance match method. In this section, the effectiveness and accuracy of the theoretical analytical solution in this paper are verified by numerical simulation. In the numerical simulation, the Runge-Kutta method is used to solve the numerical response of the nonlinear galloping energy harvester. Then, the results are compared with the analytical solution to ascertain the accuracy of the analytical solution. Since the electromechanical coupling of the system has a great influence on the maximum power, the analytical solutions are considered under different coupling conditions in the comparison.

The galloping energy harvester can be connected with various types of interface circuits in previous studies. For simplification, this paper considers the most typical AC

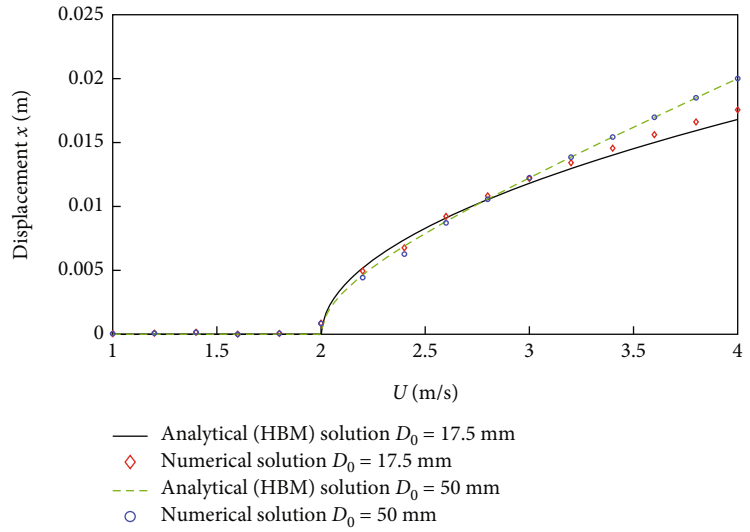

Figure 3: Comparison of the harvested power of the monostable GPEH obtained by HBM and numerical simulation.

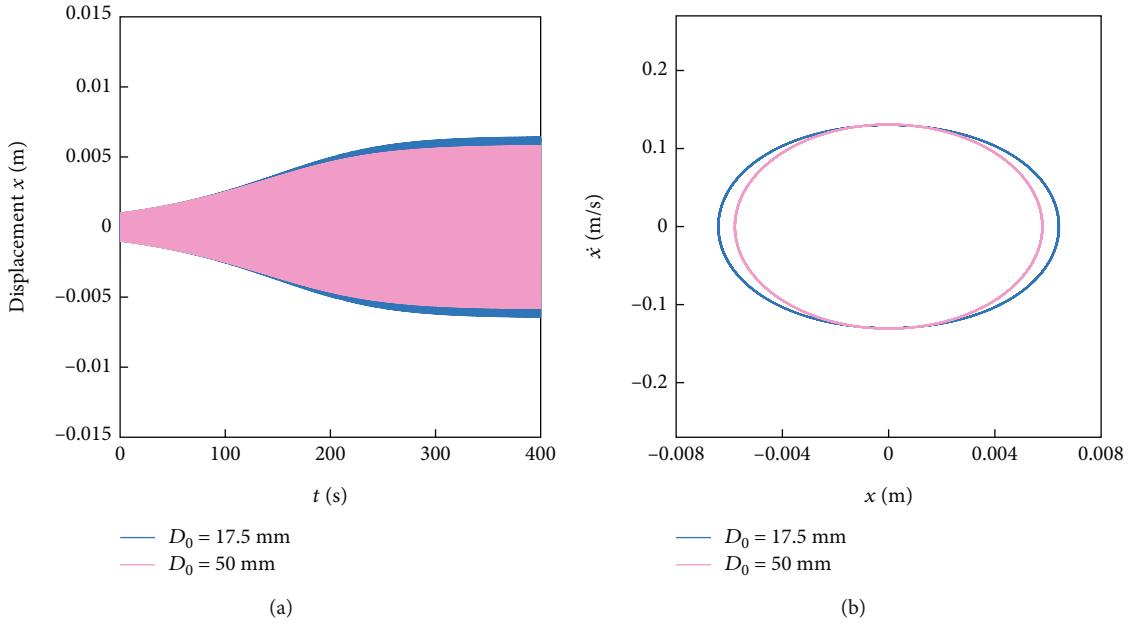

Figure 4: (a) Time domain response diagram of the system at $U = 2.3$ m/s. (b) Phase diagram at $U = 2.3$ m/s.

circuit. The system parameters used in this paper are the same as Ref. [25, 33], as shown in Table 1. There is only one load resistance R in the interface circuit. The relationship between R_{elec} and load resistance R in AC circuit [33] is shown in the following equation:

$$R_{elec}^{AC} = \frac{R}{1 + (\omega C_p R)^2}. \tag{23}$$

As shown in Figure 6, R_{elec} has a maximum value as the load resistance R increases. It can be seen from Eq. (19) that the output power of the system can reach the power limit only when Eq. (21) is satisfied. When the parameters (ρ, L, D, U, s_1, C, and θ) are determined, R_0 is a constant value. Although R_{elec} varies with the resistance R of the load circuit, it is still unclear whether its range of values can satisfy Eq. (21) or not. Hence, the value of maximum R_{elec} is of great significance. By comparing it with R_0, it can be clearly seen whether the system can achieve maximum output power or not.

Figure 7(a) gives the effect of load resistance R on output power, resistance R_{elec}, and the difference between R_0 and R_{elec}. Meanwhile, the analytical power limit, maximum

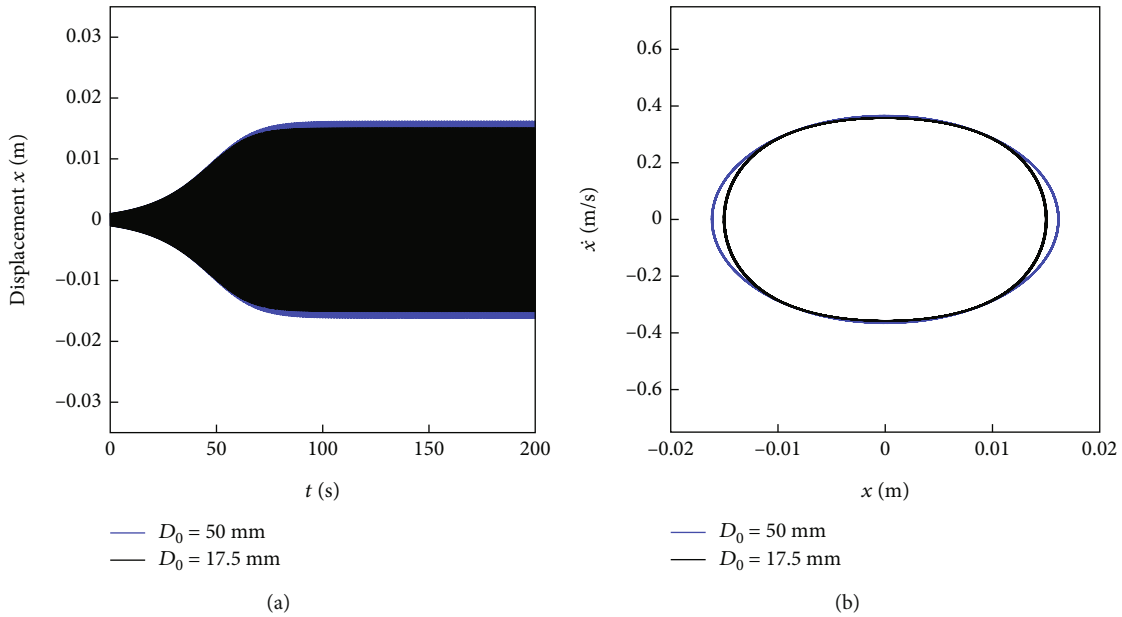

Figure 5: (a) Time domain response diagram of the system at $U = 3.5$ m/s. (b) Phase diagram at $U = 3.5$ m/s.

Table 1: System parameter.

Effective mass, M (kg)	0.1134
Effective stiffness, K (N/m)	58.02
Damping ratio, ζ	0.003
Capacitance, C_p (nF)	187
Bluff body height, L (m)	0.1
Cross-flow dimension, D (m)	0.05
Air density, ρ (kg/m^3)	1.24
Linear aerodynamic coefficient, s_1	2.5
Cubic aerodynamic coefficient, s_3	130
Magnitudes of magnetization vectors, $\bar{m}_A$ and $\bar{m}_B$ (A/m)	0.955×10^6
Volume of magnets, $\bar{v}_A$ and $\bar{v}_B$ (mm^3)	48π
Vacuum permeability, μ_0 (H/m)	$4\pi \times 10^{-7}$

output power, and R_0 are also provided. The wind speed in this case is 4 m/s. In the case of weak coupling ($\theta = 2.3 \times 10^{-4}$ N/V), R_{elec} is always smaller than R_0 and the output power is always below the power limit regardless of the change in load resistance R. Clearly, an increase in the output power P is accompanied by an increase of resistance R_{elec} and a decrease of $R_0 - R_{elec}$. When R is 230 kΩ, the difference between R_0 and R_{elec} reaches its minimum value and the corresponding output power reaches its maximum of 0.7767 mW. This feature can be explained by Eq. (19). From Eq. (19) and Figure 3, it can be obtained that the value of R_{elec} will get close to but not reach R_0 with the increase of R. Until the difference between R_0 and R_{elec} is the minimum, the output power reaches the maximum. Obviously, the maximum power is also lower than the power limit. The analytical maximum output power calculated by Eq. (19) is the same as the solution of numerical simulation.

Figure 7(b) shows the power characteristics of the GPEH under critical coupling configuration. It shows that when R reaches 230 kΩ, the maximum value of R_{elec} is 118 kΩ, which is exactly equal to R_0. The numerical maximum power also reaches the maximum value of 0.8062 mW when R_{elec} equals R_0. The result of the numerical maximum power is equal to the analytical power limit. The analytical power limit and maximum power here are obtained by Eq. (19). It is observed from Eq. (19) and Figure 6 that when the maximum value of R_{elec} is exactly equal to R_0, the maximum output power of the system is just enough to reach the power limit. Therefore, the maximum power of the numerical solution is in agreement with the maximum power and power limit of the analytical solution when the system is critically coupled.

However, when the system is strongly coupled, the power performance is completely different. It can be seen from Figure 7(c) that R_{elec} increases first and then decreases as load resistance R increasing and its maximum is larger than R_0. Hence, with the increase of load resistance R, R_{elec} equals R_0 twice and the output power reaches its maximum value twice correspondingly. Meanwhile, the analytical power limit and maximum power obtained by Eq. (19) are also shown in Figure 7(c). It can be calculated from Eq. (19) that the maximum output power of the system equals the power limit when the piezoelectric coupling coefficient is large enough. The analytical solutions of maximum power and power limit are the same. As can be observed from Figure 7(c), the values of the numerical maximum power, the analytical maximum, and the analytical power limit are equal. It should be mentioned that R_{elec} equals R_0 twice as R increases. The first power peak is at $R = 115$ kΩ and the second power peak is at $R = 495$ kΩ. This phenomenon can be expected from Eq. (19). Because once the maximum R_{elec} is greater than R_0, the value of it can be equal to R_0

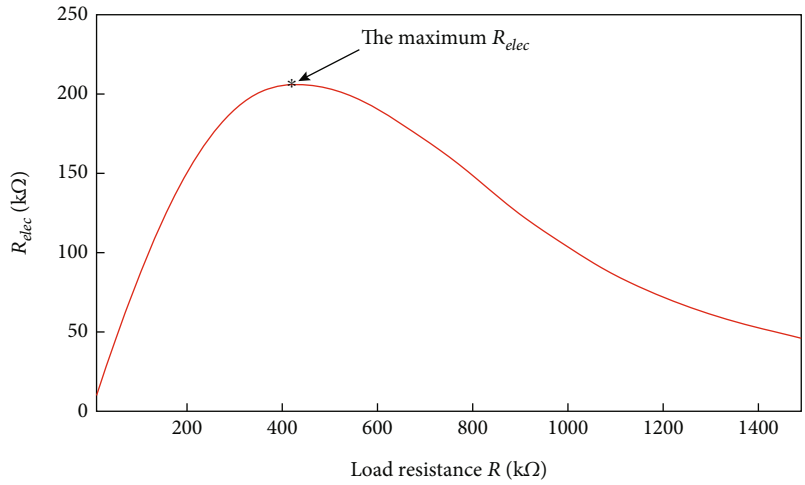

FIGURE 6: R_{elec} versus load resistance R in AC circuit.

twice as R increasing; hence, the output power can reach its maximum (power limit) 0.8062 mW twice correspondingly. Therefore, under the strong coupling condition, the theoretical method in this paper has also proved to be effective. To sum up, the numerical result is in agreement with the theoretical result for all three different coupling configurations above.

Figures 7(a)–7(c), respectively, discuss and analyze the power characteristics of the system under weak coupling configuration, critical coupling configuration, and strong coupling configuration. It is obvious that the change in the electromechanical coupling coefficient of the system has a significant effect on the performance. Figure 7(d) further illustrates the effect of the electromechanical coupling coefficient on the optimal resistance of the system. Obviously, when the electromechanical coupling coefficient is smaller than the critical coupling coefficient, there is only one optimal resistance and the system is weakly coupled. When the electromechanical coupling coefficient of the system increases to the critical coupling coefficient, it means that the maximum power reaches the power limit. As the electromechanical coupling coefficient continues to increase, the system has two optimal resistances. The reason can be found in Figure 7(c) that for a strongly coupled configuration, the maximum power reaches the maximum power twice with two different optimal resistances.

4. Power Performance Analysis

4.1. Critical Electromechanical Coupling. In the previous section, the approximate analytical solution has been obtained based on the impedance matching method and its accuracy has been well validated by numerical simulation. Therefore, the obtained analytical solution can be used to evaluate the power performance of this nonlinear galloping-based energy harvester. This section focuses on the potential benefits of stiffness nonlinearity on power performance, including critical coupling, maximum power, power limit, and optimal resistance. The maximum power, power limit, and optimal resistance have been derived in the previous section. The approximate analytical solution of the electromechanical coupling coefficient can be found as follows:

Rewrite Eq. (23) as follows:

$$R_{\text{elec}}^{AC} = \frac{1}{1/R + \left(\omega C_{\text{p}}\right)^2 R}. \tag{24}$$

According to the basic inequalities, the denominator of Eq. (23) can be written as

$$\frac{1}{R} + \left(\omega C_{\text{p}}\right)^2 R \geq 2\omega C_{\text{p}}. \tag{25}$$

When $R = 1/\omega C_{\text{p}}$, we have$1/R + (\omega C_{\text{p}})^2 R = 2\omega C_{\text{p}}$. Therefore,

$$R_{\text{elec}}^{\text{AC}} \leq \frac{1}{2\omega C_{\text{p}}}. \tag{26}$$

The maximum of $R_{\text{elec}}^{\text{AC}}$

$$\left(R_{\text{elec}}^{\text{AC}}\right)_{\max} = \frac{1}{2\omega C_{\text{p}}}. \tag{27}$$

It can be seen from expression (27) that R_{elec} has a maximum value, which is consistent with the result in Figure 6. When $R = 1/(\omega C_p)$, R_{elec} can reach its maximum $1/(2\omega C_p)$. From Eq. (21), it is learned that when the resistance R is equal to R_0, the output of the system can reach the power limit.

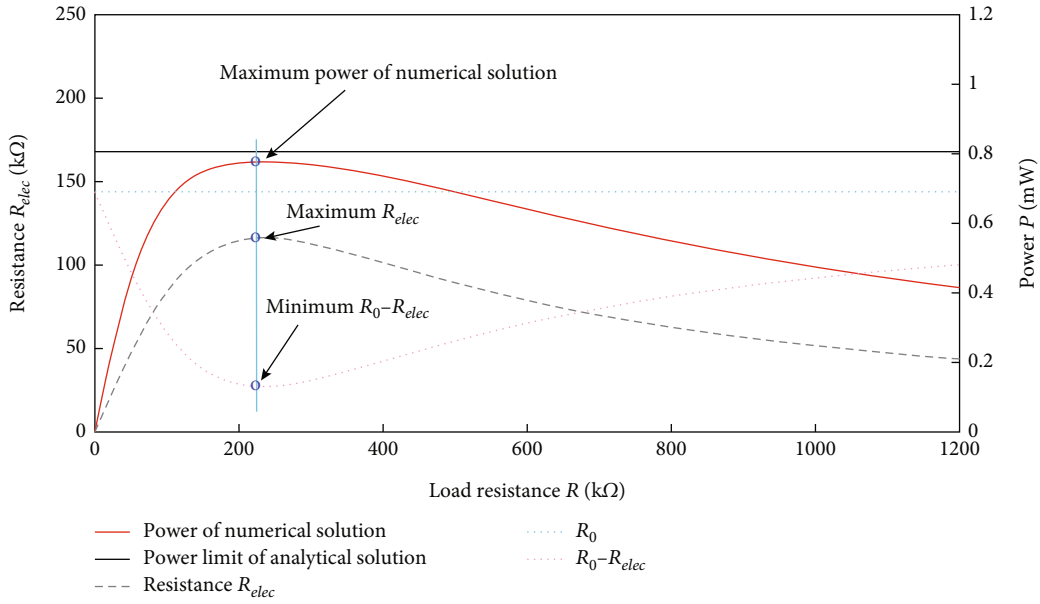

(a)

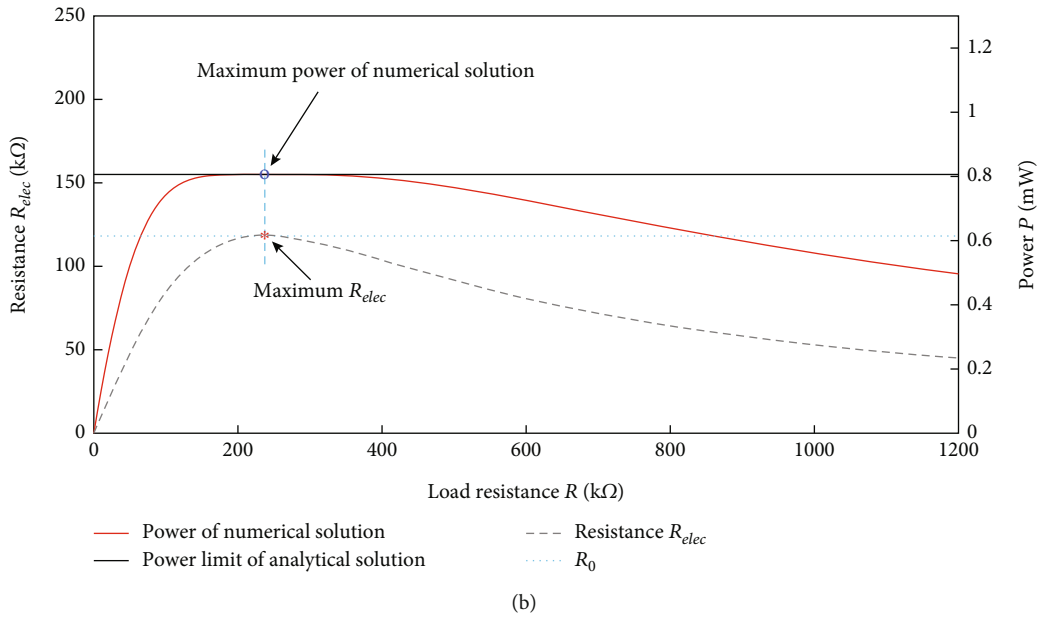

(b)

Figure 7: Continued.

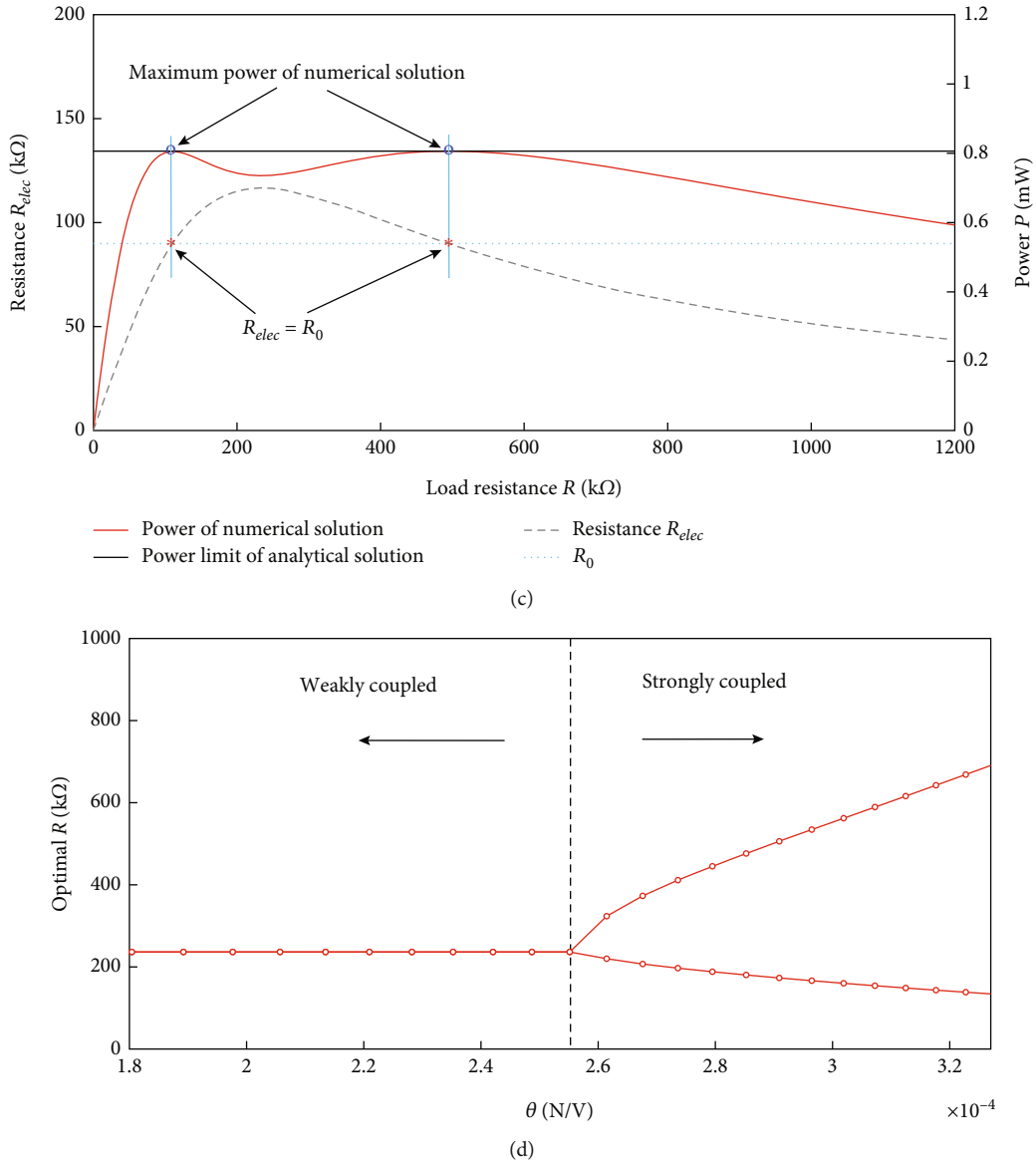

Figure 7: (a) Variations of resistance R_{elec} and output power P with the load resistance R for weak coupling configuration ($\theta = 2.3 \times 10^{-4}$ N/V). (b) Variations of resistance R_{elec} and output power P with the load resistance R for critical coupling configuration ($\theta = 2.55 \times 10^{-4}$ N/V). (c) Variations of resistance R_{elec} and output power P with the load resistance R for strong coupling configuration ($\theta = 2.9 \times 10^{-4}$ N/V). (d) Variations of the optimal resistance with the electromechanical coupling coefficient.

Substituting Eq. (21) into Eq. (26), it can be obtained that

$$\frac{\rho LDUs_1 - 2C}{4\theta^2} \leq \frac{1}{2\omega C_p}. \tag{28}$$

Equation (28) can be rewritten as

$$\theta^2 \geq \frac{\omega C_p(\rho LDUs_1 - 2C)}{2}. \tag{29}$$

Equation (29) demonstrates that the electromechanical coupling coefficient θ has a critical value, only when its value is greater than the critical one, R_{elec} can reach R_0 and the power limit can be obtained. The approximate analytical solution of the electromechanical coupling coefficient can be found as follows:

$$\theta_c = \sqrt{\frac{\omega C_p(\rho LDUs_1 - 2C)}{2}}. \tag{30}$$

The critical electromechanical coupling coefficient of the system can be calculated through Eq. (30). When the electromechanical coupling coefficient of the system is smaller than the critical coupling coefficient, the system is weakly coupled, and when the critical coupling coefficient is larger than the critical coupling coefficient, the system is strongly coupled. When the two values are equal, the system is a

critical coupled one. Here, the ratio of the electromechanical coupling coefficient θ to the critical coupling coefficient θ_c is defined as the relative electromechanical coupling degree. Equation (30) reveals that the critical electromechanical coupling coefficient θ_c depends on the system frequency ω and the wind speed U when the system parameters (ρ, L, D, U, s_1, C, and C_p) are determined. The introduction of structural nonlinearity $f_n = k_1 x + k_3 x^3$ will definitely change the frequency ω. Here, the first equation of Eq. (17) can be rewritten as

$$\omega^2 M - \left(K + k_1 + \frac{3}{4} k_3 r^2\right) + \theta^2 \omega X_{\text{elec}} = 0. \tag{31}$$

To approximately evaluate the effect of structural nonlinearity on the response frequency of a galloping system, the electrical part is ignored here. Here, Eq. (31) can then be written as

$$\bar{\omega}^2 M - \left(K + k_1 + \frac{3}{4} k_3 r^2\right) = 0. \tag{32}$$

To distinguish from ω in Eq. (31), the approximate system response frequency calculated from Eq. (32) is denoted as $\bar{\omega}$ here. It is worth noting that not considering the electrical part certainly causes some deviation in the calculation results. In order to figure out the error caused by such approximate calculation on response frequency ω, Eqs. (31) and (32) are numerically solved under different wind speeds and different electromechanical coupling situations. In the calculation, two sets of wind speeds were selected: 3 m/s and 5 m/s, and electromechanical coupling coefficients are as shown in Table 2, and the resistance R was set to 1200 kΩ. The remaining parameters not specified are detailed in Table 1. The calculation results are shown in Table 2.

Table 2 demonstrates the response frequency values calculated by Eqs. (31) and (32) at different wind speeds and different electromechanical coupling conditions and the errors of the numerical results between the two equations. At both wind speeds, the error between the approximate calculation and the exact result is relatively smaller when the electromechanical coupling is weak than when the electromechanical coupling is strong. With the increase in wind speed, the error also increases slightly. Overall speaking, the error caused by the approximate calculation is very limited. It can be inferred that the system response obtained from the approximate calculation without considering the electrical part is reliable. Hence, the power performance of the galloping-based energy system can be further studied and analyzed on this basis. Then, we can approximate the response frequency of the system as

$$\omega \approx \sqrt{\frac{K + k_1 + (3/4) k_3 r^2}{M}}. \tag{33}$$

It can be learned from Eq. (33) that the nonlinear coefficients k_1 and k_3 affect the response frequency of the system. From the previous researches [38, 41], it is known that k_1 is negative and k_3 is positive. Thus, k_1 reduces the stiffness of the system and k_3 increases it. Hence, it can be roughly judged that when the system response amplitude r is small, k_1 plays a dominant role, then the system stiffness decreases and the response frequency decreases accordingly. When the system amplitude r increases to a certain extent, k_3 plays a more significant role, thus leading to the system stiffness and response frequency increase. It can be seen that the response frequency of the system is not only related to nonlinear factors but also affected by the amplitude of the system response. The amplitude of the system response depends on the wind speed U. The higher the wind speed, the greater the response amplitude. In other words, when the wind speed is relatively small, the introduction of nonlinearity will decrease the system response frequency. When the wind speed is high, the system response frequency will be increased due to the structural nonlinearity. Therefore, to fully ascertain the influence of structural nonlinearity on the power performance of GPEH, it is reasonable to study the power performance of the nonlinear system at low and high wind speeds, respectively.

4.2. Power Performance at Low Wind Speed. In this section, the influence of nonlinearity on power characteristics under different electromechanical coupling strengths at low wind speed is explored. The distance D_0 between the magnets is set to be 16 mm and 17.5 mm, respectively, and the corresponding nonlinear coefficients k_1 and k_3 are -15 N/m, 1.9×10^5, -24 N/m, and 3.5×10^5 N/m^3, respectively. The remaining system parameters not specified are shown in Table 1.

Figure 8 shows the variation of the optimal resistance value and maximum output power of the GPEH with the electromechanical coupling coefficient at $U = 2.3$ m/s. The optimal resistance and output power of the linear system are also given. First, for the linear configuration, the critical coupling coefficient θ_c equals 1.02×10^{-4} N/V. When $\theta < \theta_c$, there is only one optimal resistance, and the maximum power is lower than the power limit. When $\theta > \theta_c$, two optimal resistances are observed, and the maximum power reaches the power limit. Similar characteristics can also be found in the nonlinear configuration. For example, the critical coupling coefficient of the nonlinear configuration with $D_0 = 17.5$ mm is 9.6×10^{-5} N/V. When $\theta < 9.6 \times 10^{-5}$ N/V, the system is weakly coupled and has one optimal resistance. Its maximum power is lower than the power limit under weakly coupled condition. As the electromechanical coupling coefficient is large enough ($\theta > 9.6 \times 10^{-5}$ N/V), the system turns out to be a strongly coupled one with two optimal resistances. The main difference between the linear and nonlinear configurations is the critical coupling coefficient. For the nonlinear GPEH with $D_0 = 17.5$ mm, its critical coupling coefficient is 9.6×10^{-5} N/V, which is lower than that of its linear counterpart. When the structural nonlinearity is enhanced ($D_0 = 16$ mm), the critical coupling coefficient further decreased to 9.32×10^{-5} N/V. From the perspective of maximum power, it can be clearly seen in Figure 1(b) that structural nonlinearity can increase the generated power of a weakly coupled GPEH and achieve the power limit with a

Table 2: Comparison of the response frequency obtained from Eqs. (30) and (31).

Case	U	θ	$\bar{\omega}$ (Hz)	ω (Hz)	Discrepancy
1	3 m/s	1.5×10^{-4} N/V	23.4438	23.4673	-0.1%
2	3 m/s	2.1×10^{-4} N/V	20.4981	20.5466	0.24%
3	5 m/s	2.5×10^{-4} N/V	34.1179	34.1624	-0.13%
4	5 m/s	2.9×10^{-4} N/V	33.9137	33.9996	-0.25%

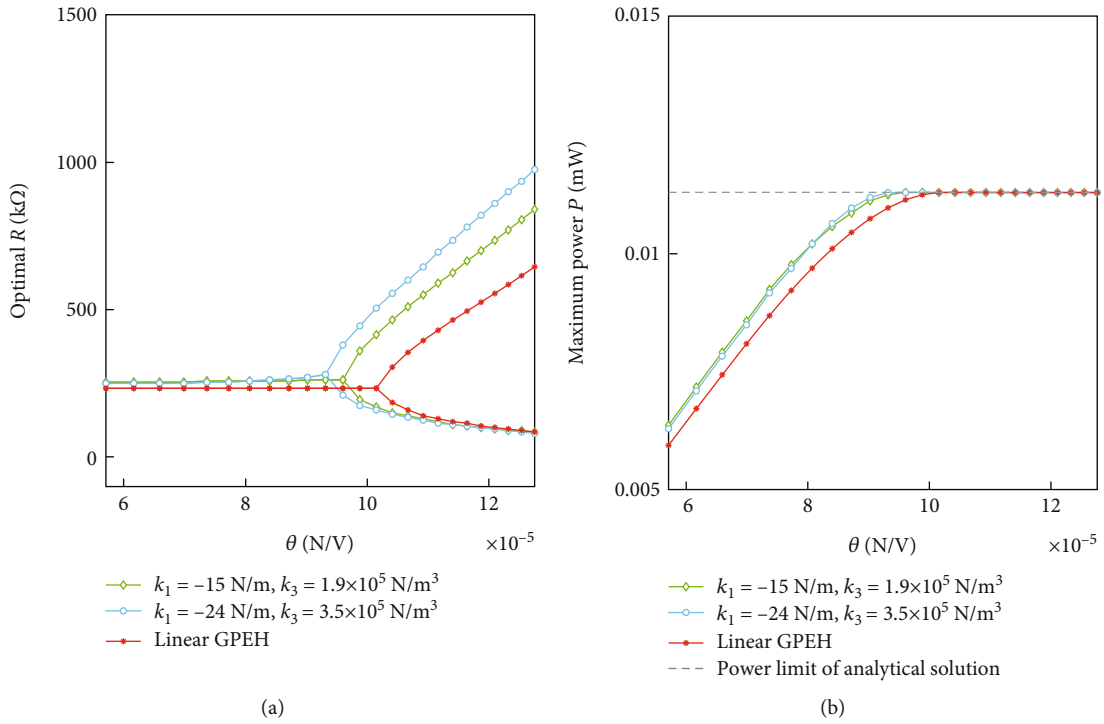

Figure 8: (a) Optimal R versus electromechanical coupling coefficient θ with different k_1 and k_3. (b) Maximum power versus electromechanical coupling coefficient θ with different k_1 and k_3 ($U = 2.3$ m/s).

small electromechanical coupling coefficient. For example, when $\theta = 8.72 \times 10^{-5}$ N/V, the maximum power of the linear configuration is about 10.43 μW, while the nonlinear configuration with $D_0 = 17.5$ mm is 10.84 μW. When the structural nonlinearity is enhanced ($D_0 = 16$ mm), the maximum power reaches the power limit, about 10.95 μW. In summary, the structural nonlinearity can effectively reduce the critical electromechanical coupling coefficient of the system and improve maximum power under weak coupling condition at low wind speed.

It can be observed from the aforementioned findings that the introduction of nonlinear stiffness at low wind speeds can significantly enhance the power characteristics of a weakly coupled system, whereas it hardly improves the power characteristics of a strongly coupled one. Therefore, in order to undertake a thorough investigation into the effects of introducing nonlinear stiffness on the power characteristics of a GPEH under low wind conditions, two specific sets of parameters corresponding to weak and strong coupling configurations were selected. θ equals 9.3×10^{-5} N/V at weak coupling configuration and it is 1.0×10^{-4} N/V at strong coupling configuration. And D_0 is set to be 17.5 mm and 16 mm, and the first set $k_1 = -15$ N/m and $k_3 = 1.9 \times 10^5$ N/m^3 the second set $k_1 = -24$ N/m and $k_3 = 3.5 \times 10^5$ N/m^3. For other parameters not specified, refer to Table 1.

4.2.1. Weakly Coupled Configuration. Figure 9 compares the output power of a nonlinear GPEH with that of its linear counterpart under a weak coupling configuration. When D_0 is 16 mm and the nonlinear coefficients are $k_1 = -15$ N/m and $k_3 = 1.9 \times 10^5$ N/m^3, respectively, the maximum power is 0.01126 mW as resistance R increases to 230 kΩ. When the output power P reaches its maximum, for comparison, the maximum power of its linear counterpart reaches 0.01096 mW with the optimal R being 230 kΩ. When the nonlinearity is strengthened ($D_0 = 16$ mm, $k_1 = -24$ N/m, and $k_3 = 3.5 \times 10^5$ N/m^3), the power characteristics change to be like that of a strongly coupled one as shown in Figure 7(b). The maximum power reaches the

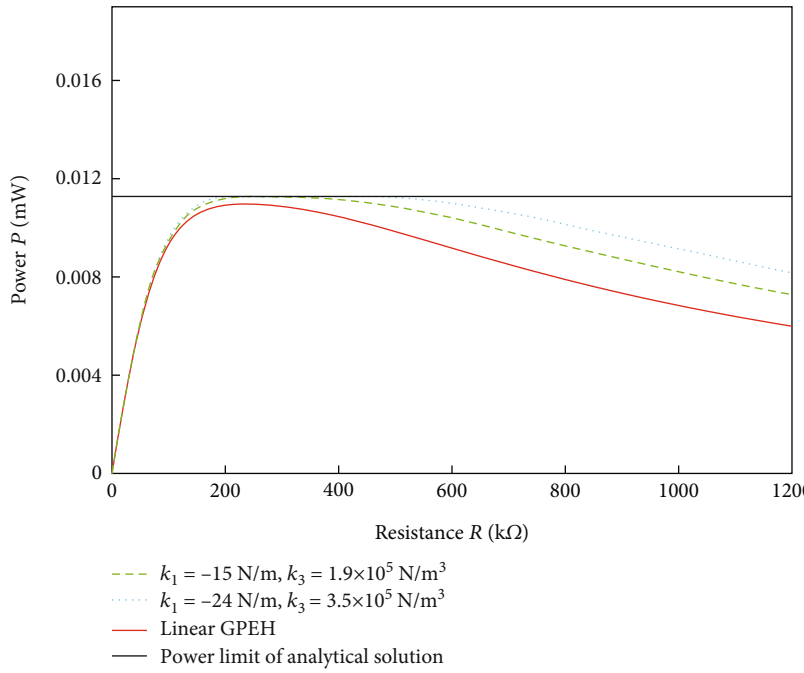

FIGURE 9: Variations of output power P with the load resistance R with different k_1 and k_3 under weak coupling configuration ($\theta = 9.3 \times 10^{-5}$ N/V).

power limit of 0.01128 mW when R equals 220 kΩ and 440 kΩ, respectively. This phenomenon means the nonlinear magnetic repulsion force makes the system turn from a weakly coupled one to a strongly coupled one. At this time, the maximum power reached the analytical power limit. It is revealed that the introduction of the nonlinear magnetic repulsion force not only increases the output power but also changes the coupling configuration when the nonlinearity is strong enough. These interesting phenomena can be explained from two different perspectives. On one hand, it can be deduced from Eq. (23) that the decline of system frequency can lead to the increase of R_{elec}. With the introduction of nonlinearity, the maximum power increases before the maximum value of R_{elec} equals R_0. The system is still in a weakly coupled state. However, when the nonlinearity is strong enough, the maximum value of R_{elec} can exceed R_0, at which point the system is changed to be a strongly coupled one and the maximum power can reach the power limit. On the other hand, the response frequency decreases after the introduction of nonlinear magnetic repulsion force at low wind speed, as shown in Figure 10. Hence, according to Eq. (29), the critical electromechanical coupling coefficient also decreases correspondingly. Therefore, the relative coupling degree of the system is increased, and the output power is increased accordingly.

4.2.2. Strongly Coupled Configuration. Figure 11 shows how the structural nonlinearity influences the power performance when it is strongly coupled at low wind speed. When D_0 is 17.5 mm and the nonlinear coefficients k_1 and k_3 are -15 N/m and 1.9×10^5 N/m^3, the maximum power reaches the power limit 0.01128 mW twice when R equals 140 kΩ and 490 kΩ, respectively. After the power reaches its maximum for the first time at $R = 140$ kΩ, the output power first decreases and then reaches its maximum again at $R = 490$ kΩ. Meanwhile, the maximum power of its linear counterpart reaches the power limit of 0.01128 mW twice when the optimal R equals 180 kΩ and 280 kΩ. When D_0 gets smaller to 16 mm and the nonlinear coefficients k_1 and k_3 equal -24 N/m and 3.5×10^5 N/m^3, respectively, the maximum output power is still 0.01128 mW when R equals 140 kΩ and 560 kΩ, respectively. Firstly, it can be seen that the nonlinear coefficients k_1 and k_3 do not affect the power limit, which is the same as the analytical result. This indicates that the nonlinear coefficients do not have an influence on the power limit although they can affect the maximum power of the system at weakly coupled configuration. Secondly, with the increase of k_1 and k_3, the first peak of the output power shifts to the left and the second to the right. In the region between these two peaks, the output power decreases significantly. Outside this region, the output power is increased. It can be obtained from the curves of R_{elec} and R_0 in Figure 7(c) and the expression of R_{elec} in Eq. (23) that the maximum R_{elec} increases with the structural nonlinearity and the interval where R_{elec} is greater than R_0 is widened accordingly. In this interval, the greater the structural nonlinearity, the greater the difference between R_{elec} and R_0. Hence, the increase in nonlinearity in this interval reduces the power. While outside this interval, enhanced nonlinearity will result in a decrease in the difference between R_{elec} and R_0, thus improving the output power.

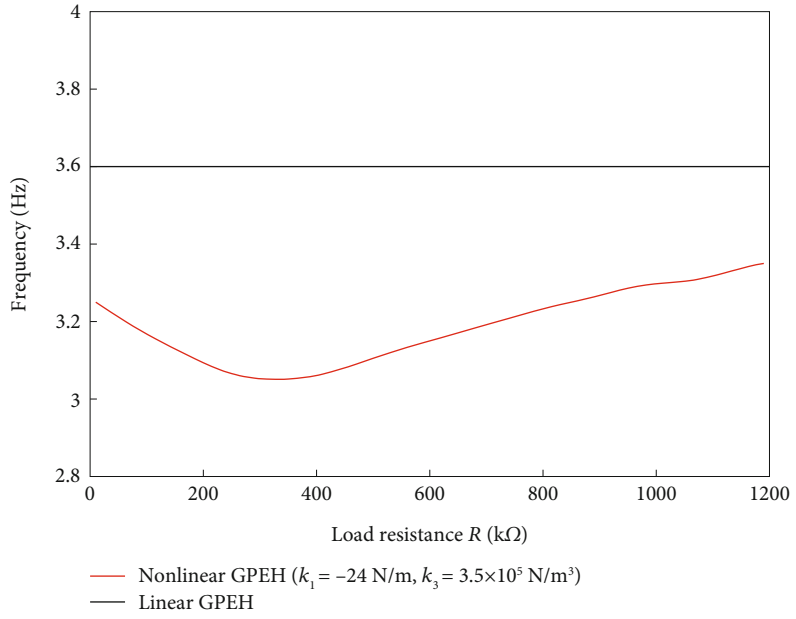

Figure 10: The frequency of nonlinear GPEH at low wind speed ($\theta = 9.3 \times 10^{-5}$ N/V).

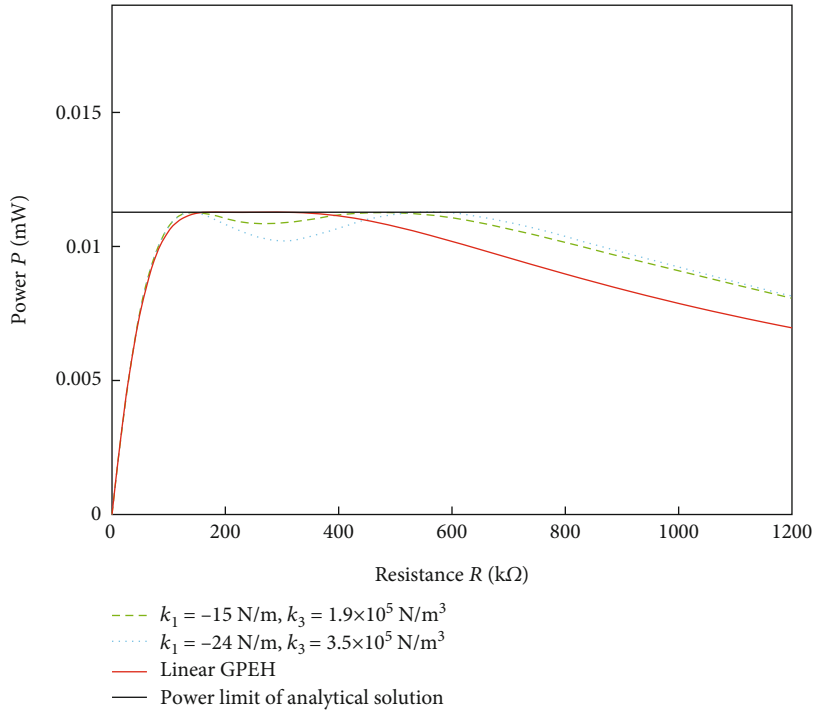

Figure 11: Variations of output power P with the load resistance R with different k_1 and k_3 under strong coupling configuration ($\theta = 1.0 \times 10^{-4}$ N/V).

4.3. Power Performance at High Wind Speed. In this section, the influence of nonlinearity on the system power characteristics under high wind speed will be explored. First, the effect of electromechanical coupling coefficients on maximum power and optimum resistance is studied.

Figure 12 depicts the effect of electromechanical coupling coefficients on maximum power and optimum resistance at high wind speed. It is found that the relation between the electromechanical coupling and the optimal resistance at high wind speed is similar to that at low wind speed. When $\theta > \theta_c$, the system becomes strongly coupled and has two optimal resistances. Otherwise, the system only has one optimal resistance. However, it is found that the effect of structural nonlinearity on the critical coupling

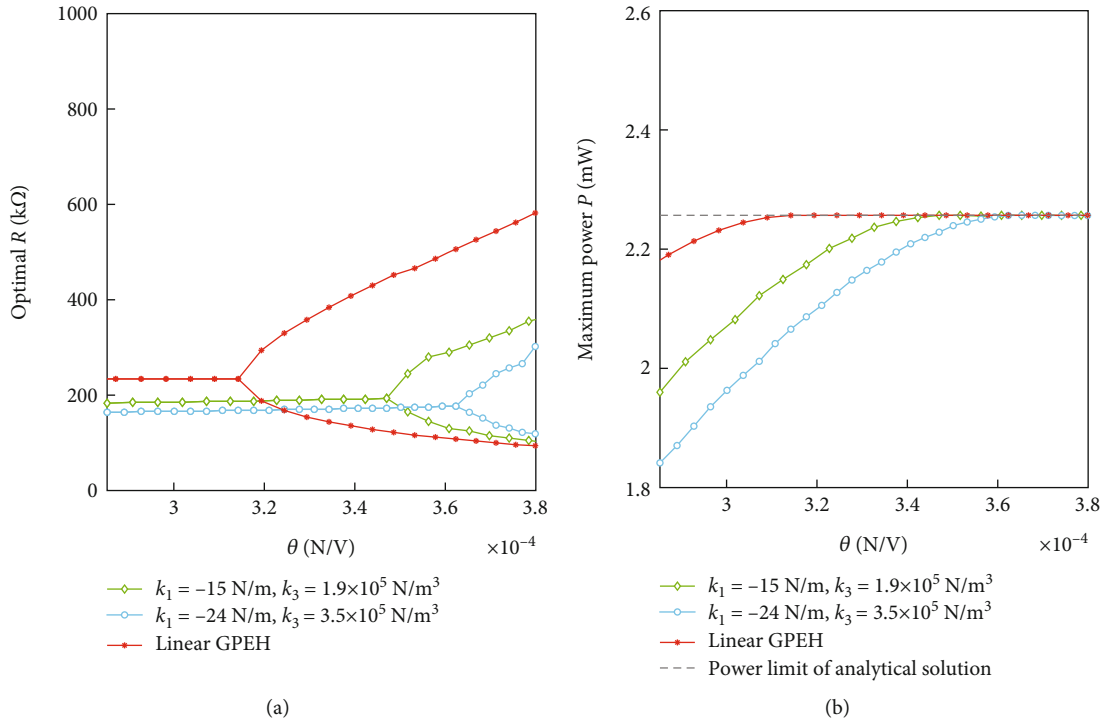

FIGURE 12: (a) Optimal R versus electromechanical coupling coefficient θ with different k_1 and k_3. (b) Maximum power versus electromechanical coupling coefficient θ with different k_1 and k_3 ($U = 5$ m/s).

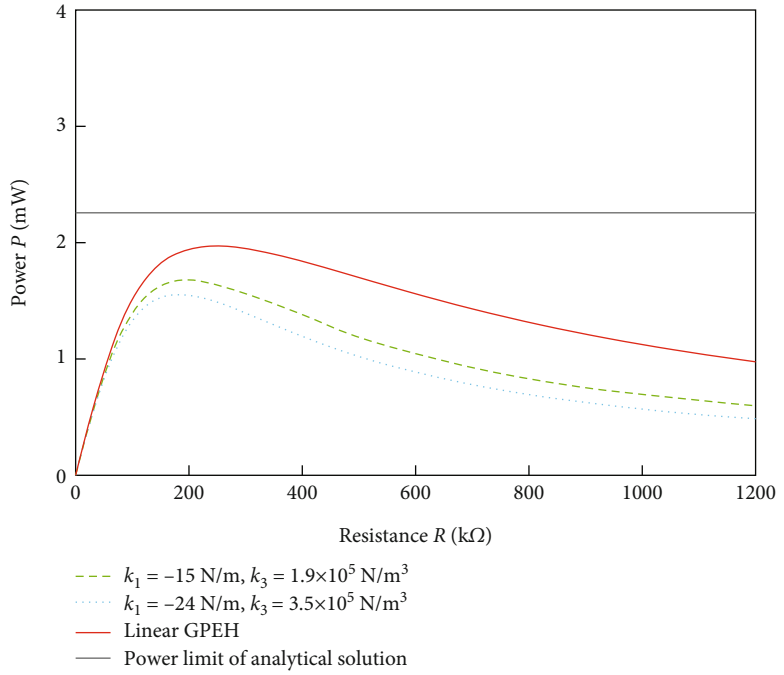

FIGURE 13: Variations of output power P with the load resistance R with different k_1 and k_3 under weak coupling configuration ($\theta = 2.6 \times 10^{-4}$ N/V).

coefficient and the maximum power at high wind speed is quite different from that at low wind speed. For instance, θ_c of linear configuration at $U = 5$ m/s is 3.14×10^{-4} N/V, while that of the nonlinear configuration with $D_0 = 17.5$ mm is 3.47×10^{-4} N/V. When the structural nonlinearity is further enhanced ($D_0 = 16$ mm), θ_c increases to $3.62 \times$

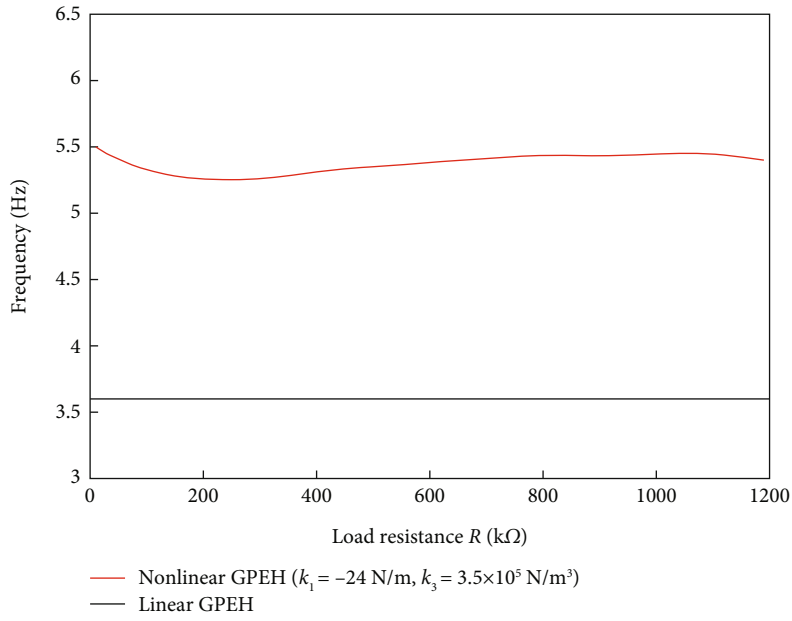

FIGURE 14: The frequency of nonlinear GPEH under high wind speed ($\theta = 2.6 \times 10^{-4}$ N/V).

10^{-4} N/V. As a result, the maximum power under a small electromechanical coupling coefficient decreases significantly with the introduction of structural nonlinearity. For instance, when $\theta = 3.04 \times 10^{-4}$ N/V, the maximum power of a linear GPEH is 2.245 mW, while that of the nonlinear configuration with $D_0 = 17.5$ mm is 2.132 mW. When D_0 is decreased to 16 mm, the maximum power further decreased to 1.974 mW. In summary, at high wind speed condition, the introduction of structural nonlinearity will significantly increase the critical electromechanical coupling coefficient, leading to a large decrease in the maximum power of a weakly coupled GPEH.

The introduction of structural nonlinearity has a completely different impact on the power characteristics of a monostable GPEH at high wind speed compared to that at low wind speed. Structural nonlinearity can lead to poorer performance of a weakly coupled GPEH at high wind speeds, while the impact on a strongly coupled one is relatively small. In order to explore the reasons for this phenomenon, two different electromechanical coupling coefficients corresponding to different coupling conditions are selected for further study. θ equals 2.6×10^{-4} N/V and 3.6×10^{-4} N/V for weakly coupled configuration and strongly coupled configuration, respectively. The system parameters unmentioned are the same as those of low wind speed.

4.3.1. Weakly Coupled Configuration. It is demonstrated in Figure 13 that the consequence of introducing structural nonlinearity into the system is a decrease in output power. When D_0 is 17.5 mm (the nonlinear coefficients $k_1 = -15$ N/m and $k_3 = 1.9 \times 10^5$ N/m^3, respectively), the maximum power is 1.679 mW and the optimal R is 200 kΩ. In comparison, the maximum power point of its linear counterpart is 1.97 mW when the optimal R equals 250 kΩ. With the strengthening of nonlinearity ($D_0 = 16$ mm, $k_1 = -24$ N/m, and $k_3 = 3.5 \times 10^5$ N/m^3), the maximum power is reduced to 1.549 mW when the optimal R is 180 kΩ. The output power and the optimal load resistance R get smaller as the nonlinear effect becomes larger. This is diametrically opposite to the system at low wind speed. It can be calculated by Eq. (28) that the increased frequency reduces the maximum R_{elec}. It leads to the difference between R_{elec} and R_0 increasing; hence, the output power is decreased. From Figure 14, it can be seen that introducing nonlinearity into a GPEH results in an increase in the frequency, which is always greater than the frequency of its linear counterpart. This indicates that when the effect of the nonlinear force is strengthened, the critical electromechanical coefficient θ_c will be increased, and the relative coupled degree will become weak. As a result, the maximum power gets reduced.

4.3.2. Strongly Coupled Configuration. When the system is strongly coupled at high wind speed ($U = 5$ m/s), the effect of the nonlinear factor is shown in Figure 15. When $D_0 = 17.5$ mm (the nonlinear coefficients $k_1 = -15$ N/m and $k_3 = 1.9 \times 10^5$ N/m^3, respectively), the maximum power is 2.257 mW with the optimal R equals 140 kΩ or 330 kΩ. Meanwhile, the maximum power point of its linear counterpart reaches the power limit of 2.257 mW twice with the optimal R equals 120 kΩ and 475 kΩ, respectively. With the strengthening of nonlinearity ($D_0 = 16$ mm, $k_1 = -24$ N/m and $k_3 = 3.5 \times 10^5$ N/m^3) the maximum power is down to 2.202 mW with the optimal R is 160 kΩ. It is obvious that with the introduction of nonlinearity, the maximum power gets declined and the system can change from a strongly coupling configuration to a critically coupling configuration or even weakly coupling configuration. This is because the enhancement of nonlinearity will lead to an increase in response frequency and critical coupling coefficient. The

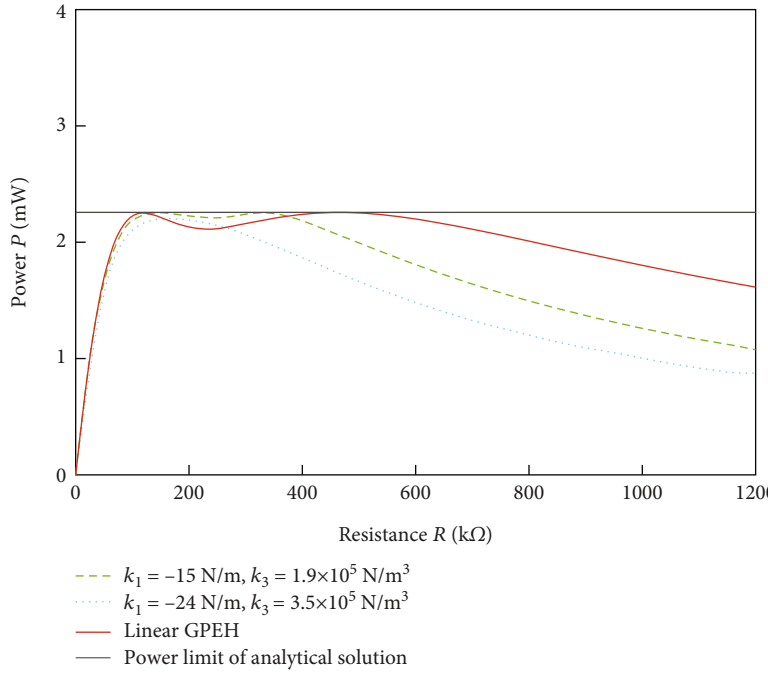

FIGURE 15: Variations of output power P with the load resistance R with different k_1 and k_3 under strong coupling configuration ($\theta = 3.6 \times 10^{-4}$ N/V).

increase in frequency can lead to a decrease in R_{elec}. When the structural nonlinearity is large enough, the maximum value of R_{elec} will be smaller than R_0, leading the system to be a weakly coupled one.

5. Conclusions

In this paper, the power characteristics of a monostable galloping energy harvester are studied. Firstly, based on the existing model, the equivalent circuit of the system is obtained by the harmonic balance method and Kirchhoff's law. The analytical solutions of the output power and the power limit are further derived. Then, the validity and accuracy of the analytical solution are verified by numerical analysis, and the critical electromechanical coupling coefficient is derived according to the analytical solution. Through analysis, it is inferred that the consequence of introducing nonlinearity can be quite different at different wind speeds. Finally, the influence of nonlinearity on the system power characteristics at low and high wind speeds is studied. Some useful conclusions are obtained as follows:

(1) For a monostable galloping-based piezoelectric energy harvester interfaced with an AC circuit, its power limit is independent of structural nonlinearity

(2) Structural nonlinearity can largely affect the critical coupling coefficients through manipulating the response frequency. For the studied structural nonlinearity $f_n = k_1 x + k_3 x^3$ (k_1 is negative and k_3 is positive), the working principle of structural nonlinearity at different wind speeds can be significantly different. At low wind speed, the system response is very weak, which makes k_1 become the dominant factor that tuning the response frequency. Since k_1 is negative, the structural nonlinearity will reduce the resonance frequency and the critical electrical coupling. As a result, at low wind speed, structural nonlinearity can make a weakly coupled system to be a strongly coupled system and is an efficient way to improve the energy harvesting performance at low wind speed condition

(3) The effect of structural nonlinearity at high wind speed is totally different from that at low wind speed. At high wind speed, k_3 becomes the dominant factor that tuning the response frequency. Since k_3 is positive, the structural nonlinearity will increase the resonance frequency and the critical electrical coupling at high wind speed. Therefore, at high wind speed, a strongly coupled system can be turned into a weakly coupled system by structural nonlinearity. As a result, at high wind speed, structural nonlinearity is not preferred in terms of output power

Overall speaking, introducing structural nonlinearity can largely affect the power performance of a galloping-based energy harvester. Different structural nonlinearity may bring in new benefits for galloping energy harvester. In this paper, it is revealed that the power performance at low wind speed is largely enhanced by the given structural nonlinearity. Notably, the theoretical study in this paper can also be used to increase the power performance at high wind speed by properly designing the structural nonlinearity.

Appendix

Derivation of the Higher-Order Harmonic Terms

Based on the assumption of the harmonic balance method, the displacement x and the speed $\dot{x}$ could be written as

$$\begin{aligned} x &= a \sin \omega t + b \cos \omega t, \\ \dot{x} &= a\omega \cos \omega t - b\omega \sin \omega t, \end{aligned} \tag{A.1}$$

where ω is the excitation frequency and a and b are unknown coefficients. The cubic power of x and $\dot{x}$ can be written in the following form:

$$\begin{aligned} x^3 &= (a \sin \omega t + b \cos \omega t)^3, \\ \dot{x}^3 &= (a\omega \cos \omega t - b\omega \sin \omega t)^3. \end{aligned} \tag{A.2}$$

Expanding the parentheses yields

$$\begin{aligned} x^3 &= a^3 \sin^3 \omega t + 3a^2 b \sin^2 \omega t \cos \omega t + 3ab^2 \sin \omega t \cos^2 \omega t + b^3 \cos^3 \omega t, \\ \dot{x}^3 &= \omega^3 \left(a^3 \cos^3 \omega t + 3ab^2 \cos \omega t \sin^2 \omega t - 3a^2 b \cos^2 \omega t \sin \omega t - b^3 \sin^3 \omega t\right). \end{aligned} \tag{A.3}$$

Then, by using the trigonometric function formula, it can be derived that

$$\begin{aligned} x^3 = {} & a^3 \left(\frac{3}{4} \sin \omega t - \frac{1}{4} \sin 3\omega t\right) + 3a^2 b \left(\frac{1}{4} \cos \omega t - \frac{1}{4} \cos 3\omega t\right) \\ & + 3ab^2 \left(\frac{1}{4} \sin \omega t + \frac{1}{4} \sin 3\omega t\right) + b^3 \left(\frac{3}{4} \cos \omega t + \frac{1}{4} \cos 3\omega t\right), \end{aligned}$$

$$\begin{aligned} \dot{x}^3 = \omega^3 \Bigg[& a^3 \left(\frac{3}{4} \cos \omega t + \frac{1}{4} \cos 3\omega t\right) + 3ab^2 \left(\frac{1}{4} \cos \omega t - \frac{1}{4} \cos 3\omega t\right) \\ & - 3a^2 b \left(\frac{1}{4} \sin \omega t + \frac{1}{4} \sin 3\omega t\right) - b^3 \left(\frac{3}{4} \sin \omega t - \frac{1}{4} \sin 3\omega t\right) \Bigg]. \end{aligned} \tag{A.4}$$

Ignoring the higher-order harmonic terms in the results, we can get the results as

$$\begin{aligned} x^3 &\approx \frac{3}{4} \left(a^3 \sin \omega t + a^2 b \cos \omega t + ab^2 \sin \omega t + b^3 \cos \omega t\right), \\ \dot{x}^3 &\approx \frac{3}{4} \omega^3 \left(a^3 \cos \omega t + ab^2 \cos \omega t - a^2 b \sin \omega t - b^3 \sin \omega t\right). \end{aligned} \tag{A.5}$$

Given r is the responding amplitude of the system and $r^2 = a^2 + b^2$, therefore

$$\begin{aligned} xr &= (a \sin \omega t + b \cos \omega t)\left(a^2 + b^2\right) \\ &= \left(a^3 \sin \omega t + a^2 b \cos \omega t + ab^2 \sin \omega t + b^3 \cos \omega t\right), \\ \dot{x}r^2 &= (a\omega \cos \omega t - b\omega \sin \omega t)\left(a^2 + b^2\right) \\ &= \omega\left(a^3 \cos \omega t + ab^2 \cos \omega t - a^2 b \sin \omega t - b^3 \sin \omega t\right). \end{aligned} \tag{A.6}$$

Comparing (A.5) and (A.6), it can be seen that the terms in parentheses are the same, so (A.5) can be simplified as

$$\begin{aligned} x^3 &\approx \frac{3}{4} r^2 x, \\ \dot{x}^3 &\approx \frac{3}{4} \omega^2 r^2 \dot{x}. \end{aligned} \tag{A.7}$$

Data Availability

The data used to support the findings of this study are included within the article.

Conflicts of Interest

The authors declared that they have no conflicts of interest in this work.

Acknowledgments

The authors would like to acknowledge the financial support from the Natural Science Foundation of China (Grant No. 12002152), Natural Science Foundation of Jiangsu Province (Grant No. BK20190379), China Postdoctoral Science Foundation Funded Project (Grant No. 2020M681577), Postgraduate Research & Practice Innovation Program of NUAA (Grant No. xcxjh20230104), and a project funded by the Priority Academic Program Development of Jiangsu Higher Education Institutions.

References

[1] Y. Zeng, R. Zhang, and T. J. Lim, "Wireless communications with unmanned aerial vehicles: opportunities and challenges," *IEEE Communications Magazine*, vol. 54, no. 5, pp. 36–42, 2016.

[2] A. Al-Qatatsheh, Y. Morsi, A. Zavabeti et al., "Blood pressure sensors: materials, fabrication methods, performance evaluations and future perspectives," *Sensors*, vol. 20, no. 16, p. 4484, 2020.

[3] Y. Gao, H. Yi, F. Li et al., "Miura-origami-structured W-tube electret power generator with water-proof and multifunctional energy harvesting capability," in *2021 IEEE 34th International Conference on Micro Electro Mechanical Systems (MEMS)*, pp. 728–731, Gainesville, FL, USA, 2021.

[4] L. Xie, G. Huang, L. Huang, S. Cai, and X. Li, "An unpowered flexible lower limb exoskeleton: walking assisting and energy harvesting," *IEEE/ASME Transactions on Mechatronics*, vol. 24, no. 5, pp. 2236–2247, 2019.

[5] H. J. Jung, A. T. Eshghi, and S. Lee, "Structural failure detection using wireless transmission rate from piezoelectric energy

harvesters," *IEEE/ASME Transactions On Mechatronics*, vol. 26, no. 4, pp. 1708–1718, 2021.

[6] X. Ma and S. Zhou, "A review of flow-induced vibration energy harvesters," *Energy Conversion and Management*, vol. 254, article 115223, 2022.

[7] J. Zhang, X. Zhang, C. Shu, Z. Fang, and Y. Ning, "Modeling and nonlinear analysis of stepped beam energy harvesting from galloping vibrations," *Journal of Sound and Vibration*, vol. 479, p. 115354, 2020.

[8] J. Wang, L. Geng, L. Ding, H. Zhu, and D. Yurchenko, "The state-of-the-art review on energy harvesting from flow-induced vibrations," *Applied Energy*, vol. 267, p. 114902, 2020.

[9] M. Bryant, E. Wolff, and E. Garcia, "Aeroelastic flutter energy harvester design: the sensitivity of the driving instability to system parameters," *Smart Materials and Structures*, vol. 20, no. 12, article 125017, 2011.

[10] L. Zhang, H. Dai, A. Abdelkefi, S. Lin, and L. Wang, "Theoretical modeling, wind tunnel measurements, and realistic environment testing of galloping-based electromagnetic energy harvesters," *Applied Energy*, vol. 254, article 113737, 2019.

[11] A. Barrero-Gil, G. Alonso, and A. Sanz-Andres, "Energy harvesting from transverse galloping," *Journal of Sound and Vibration*, vol. 329, no. 14, pp. 2873–2883, 2010.

[12] J. Sirohi and R. Mahadik, "Harvesting wind energy using a galloping piezoelectric beam," *Journal of Vibration and Acoustics*, vol. 134, no. 1, 2012.

[13] X. Li, T. Ma, B. Liu, C. Wang, and Y. Su, "Experimental study on magnetic coupling piezoelectric-electromagnetic composite galloping energy harvester," *Sensors*, vol. 22, no. 21, 2022.

[14] L. Wang, T. Tan, Z. Yan, D. Li, B. Zhang, and Z. Yan, "Integration of Tapered Beam and Four Direct-Current Circuits for Enhanced Energy Harvesting from Transverse Galloping," *IEEE/ASME Transactions on Mechatronics*, vol. 24, no. 5, pp. 2248–2260, 2019.

[15] W. Qin, W. Deng, J. Pan, Z. Zhou, W. Du, and P. Zhu, "Harvesting wind energy with bi-stable snap-through excited by vortex-induced vibration and galloping," *Energy*, vol. 189, article 116237, 2019.

[16] A. Abdelkefi, M. R. Hajj, and A. H. Nayfeh, "Power harvesting from transverse galloping of square cylinder," *Nonlinear Dynamics*, vol. 70, no. 2, pp. 1355–1363, 2012.

[17] H. Dai, A. Abdelkefi, Y. Yang, and L. Wang, "Orientation of bluff body for designing efficient energy harvesters from vortex-induced vibrations," *Applied Physics Letters*, vol. 108, no. 5, article 053902, 2016.

[18] Y. Yu, G. Yao, and Z. Wu, "Nonlinear primary responses of a bilateral supported X-shape vibration reduction structure," *Mechanical Systems and Signal Processing*, vol. 140, article 106679, 2020.

[19] Y. Yang, L. Zhao, and L. Tang, "Comparative study of tip cross-sections for efficient galloping energy harvesting," *Applied Physics Letters*, vol. 102, no. 6, article 064105, 2013.

[20] A. Abdelkefi, Z. Yan, and M. R. Hajj, "Performance analysis of galloping-based piezoaeroelastic energy harvesters with different cross-section geometries," *Journal of Intelligent Material Systems and Structures*, vol. 25, no. 2, pp. 246–256, 2014.

[21] F.-R. Liu, W.-M. Zhang, Z.-K. Peng, and G. Meng, "Fork-shaped bluff body for enhancing the performance of galloping-based wind energy harvester," *Energy*, vol. 183, pp. 92–105, 2019.

[22] X. Yang, X. He, J. Li, and S. Jiang, "Modeling and verification of piezoelectric wind energy harvesters enhanced by interaction between vortex-induced vibration and galloping," *Smart Materials and Structures*, vol. 28, no. 11, p. 115027, 2019.

[23] G. Hu, J. Wang, Z. Su, G. Li, H. Peng, and K. Kwok, "Performance evaluation of twin piezoelectric wind energy harvesters under mutual interference," *Applied Physics Letters*, vol. 115, no. 7, article 073901, 2019.

[24] H. Kim, J. Lee, and J. Seok, "Novel piezoelectric wind energy harvester based on coupled galloping phenomena with characterization and quantification of its dynamic behavior," *Energy Conversion and Management*, vol. 266, p. 115849, 2022.

[25] A. Bibo, A. H. Alhadidi, and M. F. Daqaq, "Exploiting a nonlinear restoring force to improve the performance of flow energy harvesters," *Journal of Applied Physics*, vol. 117, no. 4, article 045103, 2015.

[26] X. Huang and B. Yang, "Investigation on the energy trapping and conversion performances of a multi-stable vibration absorber," *Mechanical Systems and Signal Processing*, vol. 160, article 107938, 2021.

[27] J. Wang, L. Geng, S. Zhou, Z. Zhang, Z. Lai, and D. Yurchenko, "Design, modeling and experiments of broadband tristable galloping piezoelectric energy harvester," *Acta Mechanica Sinica*, vol. 36, no. 3, pp. 592–605, 2020.

[28] A. H. Alhadidi and M. F. Daqaq, "A broadband bi-stable flow energy harvester based on the wake-galloping phenomenon," *Applied Physics Letters*, vol. 109, no. 3, article 033904, 2016.

[29] X. Huang, "Stochastic resonance in a piecewise bistable energy harvesting model driven by harmonic excitation and additive Gaussian white noise," *Applied Mathematical Modelling*, vol. 90, pp. 505–526, 2021.

[30] X. Huang and B. Yang, "Improving energy harvesting from impulsive excitations by a nonlinear tunable bistable energy harvester," *Mechanical Systems and Signal Processing*, vol. 158, article 107797, 2021.

[31] X. Huang and B. Yang, "Towards novel energy shunt inspired vibration suppression techniques: principles, designs and applications," *Mechanical Systems and Signal Processing*, vol. 182, article 109496, 2023.

[32] X. Huang and T. Zhong, "Hydrokinetic energy harvesting from flow-induced vibration of a hollow cylinder attached with a bi-stable energy harvester," *Energy Conversion and Management*, vol. 278, article 116718, 2023.

[33] C. Lan, Y. Liao, and G. Hu, "A unified equivalent circuit and impedance analysis method for galloping piezoelectric energy harvesters," *Mechanical Systems and Signal Processing*, vol. 165, article 108339, 2022.

[34] Y. Liao and J. Liang, "Maximum power, optimal load, and impedance analysis of piezoelectric vibration energy harvesters," *Smart Materials and Structures*, vol. 27, no. 7, article 075053, 2018.

[35] Y. Liao and J. Liang, "Unified modeling, analysis and comparison of piezoelectric vibration energy harvesters," *Mechanical Systems and Signal Processing*, vol. 123, pp. 403–425, 2019.

[36] Y. Liao and H. A. Sodano, "Model of a single mode energy harvester and properties for optimal power generation," *Smart Materials and Structures*, vol. 17, no. 6, 2008.

[37] H. Yung, P. Landecker, and D. Villani, "An analytic solution for the force between two magnetic dipoles," *Physical Separation in Science and Engineering*, vol. 9, pp. 39–52, 1998.

[38] C. Lan, Y. Liao, G. Hu, and L. Tang, "Equivalent impedance and power analysis of monostable piezoelectric energy harvesters," *Journal of Intelligent Material Systems and Structures*, vol. 31, no. 14, pp. 1697–1715, 2020.

[39] L. Zhao, L. Tang, J. Liang, and Y. Yang, "Synergy of wind energy harvesting and synchronized switch harvesting interface circuit," *IEEE/ASME Transactions on Mechatronics*, vol. 22, no. 2, pp. 1093–1103, 2017.

[40] L. Zhao and Y. Yang, "Analytical solutions for galloping-based piezoelectric energy harvesters with various interfacing circuits," *Smart Materials and Structures*, vol. 24, no. 7, article 075023, 2015.

[41] H. Li, H. Ren, F. Cao, and W. Qin, "Improving the galloping energy harvesting performance with magnetic coupling," *International Journal of Mechanical Sciences*, vol. 237, article 107785, 2023.